Thermal transport analysis of the edge region in the low and high confinement stages of a DIII-D discharge

W. M. Stacey, Georgia Tech, Atlanta, GA 30332

and

R. J. Groebner, General Atomics, San Diego, CA 92186

August, 2006

Revised October, 2006

Abstract The ion and electron thermal diffusivities have been inferred from measured density and temperature profiles in the edge of a DIII-D [J. Luxon, , Nucl. Fusion, 42, 614 (2002)] discharge with a low confinement (L-mode) stage followed by a high confinement (H-mode) stage free of edge localized modes (ELMs). Conductive heat flux profiles used to construct the inferred thermal diffusivities were calculated taking into account heat convection, radiation, atomic physics effect of recycling neutrals, ion-electron equilibration and neutral beam heating. The inferred thermal diffusivities were compared with theoretical predictions.

PACS 52.55.Fi

I. Introduction

The physics of the steep-gradient, edge pedestal region in H-mode (high confinement mode) plasmas has been the subject of experimental investigation for many years (e.g. Refs. 1-8). The motivation for understanding the edge pedestal is based, at least in part, on calculations[9,10] which indicate that because of "stiffness" in temperature profiles the performance of future tokamaks will be sensitive to the value of the density and particularly the temperature at the top of the edge pedestal.

Theoretical efforts to understand the edge pedestal have focused on several different aspects of the underlying physics. Investigations (e.g. Refs. 11-14) of the MHD stability of the edge pressure pedestal against ballooning and peeling (surface kink) modes have led to an understanding of edge pressure/pressure gradient limits leading to the onset of edge-localized-mode (ELM) instabilities which momentarily destroy the edge pedestal structure. Several other lines of investigation[15-22] have been developed to the end of explaining (or at least modeling) the edge pedestal structure observed in the absence of or in between or averaged over ELMs.

The ion and electron thermal diffusivities are important parameters in any attempt to understand the edge temperature pedestals. Knowledge of these diffusivities to date comes almost entirely from their trial and error adjustment in transport simulations to obtain agreement with observed edge temperature profiles[7,8,16,17,19,20], although there have been some initial efforts to calculate edge thermal diffusivities from edge turbulence codes (e.g. Refs. 23 and 24).

We recently introduced a procedure to take into account the effects of radiation, atomic physics of recycling neutrals, ion-electron equilibration and convective heat fluxes in inferring thermal diffusivities from measured profiles in the plasma edge and applied that procedure to infer thermal diffusivities in several ELMing H-mode discharges[25]. Our purpose in this paper is apply the same procedure to examine the change in thermal transport between the L-mode phase and H-mode phase of a discharge with a long ELM-free H-mode. The radial variation of total and convective heat fluxes are calculated over the edge region in both the L-mode and H-mode phases. Experimental thermal diffusivities are inferred and compared with various theoretical predictions in order to investigate possible underlying transport mechanisms, without the complication of ELMs.

II. Procedure for Inference of Heat Transport Coefficients from Experiment

The total ion and electron radial heat fluxes consist of conductive and convective components

$$Q_{i,e} = n_{i,e} T_{i,e} \chi_{i,e} L_{Ti,e}^{-1} + \frac{5}{2} \Gamma_{i,e} T_{i,e} \tag{1}$$

Thus, if $n_{i,e}, T_{i,e}$ and $L_{Ti,e}^{-1}$ are determined experimentally and $Q_{i,e}$ and $\Gamma_{i,e}$ are calculated from heat and particle balances, the experimental $\chi_{i,e}$ profile can be evaluated from

$$\chi_{i,e}(r) = L_{Ti,e}(r) \left[\frac{Q_{i,e}(r)}{n_{i,e}(r) T_{i,e}(r)} - \frac{5}{2} \frac{\Gamma_{i,e}(r)}{n_{i,e}(r)} \right] \tag{2}$$

We note that this inference of $\chi_{i,e}$ depends not only on the measured temperature and density profiles and the total heat flux $Q_{i,e}$, but also on the convective heat flux.

We use an integrated modeling code system[26] that performs i) particle and power balances on the core plasma to determine the net particle and heat fluxes outward across the separatrix, which are used as input to ii) an extended 2-point divertor model (with radiation and atomic physics) that calculates plasma densities and temperatures in the divertor and SOL and the ion flux incident on the divertor plate, which iii) is recycled as neutral molecules and atoms that are transported (2D Transmission-Escape Probabilities [TEP] method, a form of kinetic integral transport theory [Ref. 26]) through the divertor region across the separatrix into the plasma edge region. Any sources of gas puffed neutrals are also similarly transported inward. This integrated code system is used to calculate the ion particle and total heat fluxes crossing the separtrix from the core into the SOL (scrape-off layer). The recycling neutral source is adjusted so that the integrated calculation yields the measured line average density in order to insure that fueling is calculated correctly.

Using these values from the integrated model calculation as separatrix boundary conditions, we can then integrate the plasma ion particle balance equation

$$\frac{\partial \Gamma}{\partial r} = -\frac{\partial n_i}{\partial t} + n_e n_o < \sigma v >_{ion} + S_{nb}, \qquad \Gamma(r_{sep}) = \Gamma_{sep}^{\exp} \tag{3}$$

across the edge region to determine the edge distributions of $\Gamma(r)$, where n_o is the density of recycling and gas fueling neutrals and S_{nb} is the source rate of plasma ions due to neutral beam (and pellet) injection. We can also integrate the heat balance equations

$$\frac{\partial Q_i}{\partial r} = -\frac{\partial}{\partial t}\left(\frac{3}{2} n_i T_i \right) + q_{nbi} - \frac{3}{2}(T_i - T_o^c) n_i n_o^c < \sigma v >_{cx+el} - q_{ie}, \quad Q_i(r_{sep}) = Q_{sepi}^{\exp} \tag{4a}$$

and

$$\frac{dQ_e}{dr} = -\frac{\partial}{\partial t}\left(\frac{3}{2} n_e T_e\right) + q_{nbe} + q_{ie} - n_e n_o < \sigma v >_{ion} E_{ion} - n_e n_z L_z, \qquad Q_e\left(r_{sep}\right) = Q_{sepe}^{\exp} \qquad (4b)$$

inward from the separatrix to determine the $Q_{i,e}(r)$ needed to evaluate the radial distribution of $\chi_{i,e}$ from Eq. (2). The boundary conditions at the separatrix were determined by modeling the experimental conditions with global particle and power balances. Here $q_{nbi,e}$ is the local neutral beam power deposition density, n_o is the recycling neutral density, n_o^c is the density of 'cold' recycling neutrals that have not yet collided inside the separatrix and $1.5T_o^c$ is their average energy, $q_{ie} \sim \left(T_i - T_e\right)/T_e^{1.5}$ is the ion-electron equilibration rate, $E_{ion}(T_e, n_e)$ is the ionization energy, n_z is the impurity (carbon) density, $L_z\left(T_e, n_o\right)$ is the impurity radiation emissivity, $< \sigma v >_{cx+el}\left(T_i\right)$ is the charge-exchange plus elastic scattering rate coefficient, and $< \sigma v >_{ion}\left(T_e, n_e\right)$ is the electron impact ionization rate coefficient. The experimental $n_{e,z}$ and $T_{i,e}$ and the calculated neutral density are used to evaluate the terms in Eqs. (3) and (4), which are then integrated radially inward from the experimental separatrix boundary conditions for the particle and heat fluxes determined as discussed above. We must at present estimate the split of Q_{sep} into Q_{sepi} and Q_{sepe}. The atomic physics data are taken from Ref. [27] (with subsequent extensions to higher temperatures), and the radiation emissivity is calculated from a fit to coronal equilibrium calculations (taking into account the effect of charge-exchange and recombination in the presence of recycling neutrals) based on the ADPAC data[28].

III. Description of ELM-free Phase of DIII-D Shot 118897

The main goal of this study was to examine the edge transport in the absence of MHD events, such as ELMs. For this purpose, a conventional H-mode discharge was produced with a long ELM-free phase by using moderately high triangularity to provide good edge MHD stability and by operating at low heating power to delay the onset of ELMs, as illustrated in Fig. 1. Analysis times were chosen centered at 1525 ms, 1640 ms and 2140 ms, corresponding to the L-mode phase, early in the H-mode phase and late in the ELM-free H-mode phase. Each profile used in the analysis is based on a composite

of experimental data obtained over a time window of 35 ms in the L-mode and 50 ms at each of the two H-mode times.

The electron temperature and density were obtained from a multi-point Thomson scattering system[29]. The electron density from this system was adjusted to match the line-averaged density from a CO2 interferometer; the adjustments were small – roughly 5% or less. Each time window in the analysis overlaps 2 to 4 pulses of the Thomson laser. The Te and ne profiles from the Thomson system were aligned in flux space in the following way. The data for each electron temperature profile were mapped to normalized psi with a magnetic equilibrium generated at the time that the data were acquired. All temperatures and flux coordinates within a time window were then grouped and fit with a function which consists of a tanh function in the pedestal which joins smoothly to a spline fit in the core. After this fit, the T_e and n_e data points and the fitted profiles were shifted in psi space by an amount required to align the foot of the tanh function for the T_e profile with the plasma separatrix. These fits and the underlying data points are shown in Fig. 2.

The ion temperature and Carbon density were obtained from measurements of the C VI 5290 line with a charge exchange recombination spectroscopy system[30]. As with the Thomson data, the data were taken from multiple frames obtained during each time window. No spatial adjustment was performed on these data. The ion temperature was fit with a spline function, and as shown in Fig. 2 this provided a good fit both in the pedestal region and in the core of the plasma. An absolute intensity calibration was used to convert the intensity measurements of the C VI ions into a carbon density. The carbon densities were divided by the electron densities to produce profiles of fractional impurity content. This function tends not to vary strongly across the plasma. It was fit with a spline function with a constraint to force the fit to be constant in about the outer 10% of the plasma radius. Typically, carbon is the dominant source of Zeff in discharges of this type. Thus, the main ion density was computed from the fits to the electron density and to the carbon fraction.

IV. Analysis of ELM-free Phase of DIII-D Shot 118897

Our purpose is to obtain a better understanding of the edge thermal transport in L-mode and in the ELM-free H-mode phase and of how they differ. For this reason, the

discussion is structured as a comparison of various quantities just before L-H, just after L-H, and well after L-H.

A. Power balance and heat flux profiles

The values of the various cooling and heating terms in Eqs. (4), evaluated using the measured density and temperatures, are shown in Figs. 3. The ion-electron energy transfer term $q_{ie} \sim (T_i - T_e)/T_e^{3/2}$ is dominant at the outer radii at all times because of the large difference between ion and electron temperatures and the small values of the electron temperature, but this term becomes much less important at inner radii where the ion and electron temperatures become comparable later in the H-mode. The charge-exchange (and elastic scattering) cooling term is important just inside the separatrix, but its profile becomes more sharply attenuated with density buildup in H-mode. The carbon radiation cooling term is almost uniform in the low T_e L-mode, but becomes peaked towards the lower T_e outer radii as the pedestal 'flattop' temperature increases in H-mode. The neutral beam (E_b = 80 keV) heating is preferentially of the electrons.

These heating and cooling rates were used in Eq. (4) to calculate the total ion and electron heat flux profiles. The transient (time derivative) terms were taken into account separately in the pedestal and the core. The global core power and particle balances were evaluated by taking $d\ln W/dt$ and $d\ln \bar{n}/dt$ from experiment, where W is the total energy content, and multiplying by $1.5nT$ and $\bar{n}$, respectively; these terms had only a small effect on the global calculation. In solving the edge particle and power balance Eqs. (3) and (4), the measured $d\ln p_{ped}/dt$ and $d\ln n_{ped}/dt$ at the top of the pedestal were multiplied by the local values of $1.5nT$ and n from the fits of Fig. 2 were used to evaluate the transient terms; these terms were significant for the early (1640ms) time in the H-mode when the pedestal density and pressure were increasing rapidly. The split between the ion and electron heat flux at the separatrix was estimated to be $f_{heate} \equiv \{Q_e/(Q_e + Q_i)\}_{in} = 0.6$.

As seen in Fig. 4, the total ion heat flux calculated from Eq. (4a) decreases with radius because of the increase in radius of the ion-electron energy transfer and of charge exchange cooling, which is not compensated by the relative small neutral beam heating of ions. The total electron heat flux calculated from Eq. (4b), on the other hand, increases with radius because the ion-electron energy transfer plus the neutral beam heating is everywhere greater than the radiation plus ionization cooling of the electrons. The

transient pedestal temperature and density increases early in the H-mode (1640 ms) reduces the outward heat and particle fluxes; in fact the particle flux (and convective heat flux) becomes negative inside the strong recycling region just inside the separatrix.

In L-mode, the convective heat flux increases with radius for the ions because of the increase in outward particle flux due to ionization of recycling neutrals. The electron heat flux does not increase much with radius because the effect of ionizing neutrals in increasing the particle flux is offset by the decreasing with radius of the electron temperature. In L-mode the particle flux, hence the convective heat fluxes, is everywhere outward (positive). On the other hand, in the early stage of the H-mode the particle flux calculated from Eq. (3) is inward (negative) except in the outer high-recycling region of the edge, as it must be to provide for the increasing plasma density over the H-mode phase of the discharge.

B. Inferred thermal diffusivities

The total and convective heat fluxes shown in Figs. 4 were used, together with the experimental gradient scale lengths determined from the fits given in Figs. 2, in Eq. (2) to infer the thermal diffusivities plotted in Figs. 5 and 6. The experimental gradient scale lengths, L_{Ti} and L_{Te}, both decreased monotonically (the gradients increased monotonically) with radius for all times (except just at the separatrix).

The most striking feature of these figures is the generally expected drop in the ion and electron thermal diffusivity between L-mode and H-mode (by an order of magnitude). The fact that this decrease occurs over the entire edge region ($0.86 < \rho < 1.0$), rather than just in a localized "transport barrier" aligned with the steepest gradient region, is notable. In fact, in the region in which the electron temperature gradient becomes steepest $\chi_e^{\exp}$ is actually becoming higher than elsewhere. This is qualitatively consistent with the substantial reductions in $\chi_{e,i}^{\exp}$ across the L-H transition that were previously inferred[31] in DIII-D discharges for regions in the plasma interior ($\rho < 0.85$). Both $\chi_e^{\exp}$ and $\chi_i^{\exp}$ are largest at the separatrix, except for $\chi_i^{\exp}$ in the early, transient phase of the H-mode (1640 ms).

C. Sensitivity studies

Consideration of the uncertainty in the determination of the thermal diffusivities 15 is in order at this point. Errors may enter the determination through the experimental

density and temperature profiles or through the calculated total and convective heat fluxes. The error bars on the measured temperatures are < 10% and on the measured densities < 5%.

The necessity of specifying the heat flux split $f_{heate} \equiv \{Q_e/(Q_e+Q_i)\}_{in}$ between ions and electrons entering the edge region from the core introduces an uncertainty into the analysis. As discussed previously[25], a physically plausible range (found previously to be centered about $f_{heate} \approx 0.5$) can be determined by the physical requirement that the convective heat flux can not exceed the total heat flux for either species (note from Fig. (4b) that $f_{heate} \approx 0.6$ is almost at this limit at 1640 ms). The entire calculation was repeated for $f_{heate} = 0.4$, and the inferred thermal diffusivities are compared in Fig. 7. Based on a previous study[25] of the range of f_{heat} for which physically plausible solutions are found, Fig. 7 is probably representative of the uncertainty in the determination of $\chi_{e,i}^{exp}$ due to the necessity of estimating f_{heat}.

Next, we examined the sensitivity of $\chi_{e,i}^{exp}$ to the spatial heat flux profile used in evaluating Eq. (2). The previous results calculated using Q(r) and Γ(r) in Eq. (2) are denoted "exp" in Figs. 8. The calculation was repeated neglecting the convective component by setting Γ = 0 in Eq. (2), with the result denoted "exp2" in Fig. 8. Then the calculation was repeated once again setting Γ = 0 and replacing the spatial profile Q(r) by the constant value of the total heat flux at the separatrix $Q(r_{sep})$, with the result being denoted "exp3" in Fig. 8. Clearly, the results are sensitive to the use of the proper spatial heat and particle flux profiles to evaluate Eq. (2).

V. Theoretical transport models

Although gyrofluid or gyrokinetic calculations of turbulent transport are probably needed to accurately represent the current theoretical understanding of transport, these generally require large-scale computer simulations, and such calculations for edge plasmas are beyond the current state-of-the-art. However, the analytical theoretical formulas commonly used in transport codes can provide useful insights.

A. Ion transport

1. Neoclassical

The Chang-Hinton neoclassical expression for the ion thermal conductivity is[32,33]

$$\chi_i^{neoch} = \varepsilon^{1/2} \rho_{i\theta}^2 \nu_{ii} \left[a_1 g_1 + a_2 (g_1 - g_2) \right] \tag{5}$$

where the a's account for impurity, collisional and finite inverse aspect ratio effects and the g's account for the effect of the Shafranov shift

$$\begin{aligned}
a_1 &= \frac{0.66(1+1.54\alpha) + \left(1.88\sqrt{\varepsilon} - 1.54\varepsilon\right)(1+3.75\alpha)}{1+1.03\sqrt{\mu_j^*} + 0.31\mu_j^*} \\
a_2 &= \frac{0.59\mu_j^*\varepsilon}{1+0.74\mu_j^*\varepsilon^{3/2}} \left[1 + \frac{1.33\alpha(1+0.60\alpha)}{1+1.79\alpha} \right] \\
g_1 &= \frac{1+\frac{3}{2}\left(\varepsilon^2 + \varepsilon\Delta'\right) + \frac{3}{8}\varepsilon^3\Delta'}{1+\frac{1}{2}\varepsilon\Delta'} \\
g_2 &= \frac{\sqrt{1-\varepsilon^2}\left(1+\frac{\varepsilon\Delta'}{2}\right)}{1+\frac{\Delta'}{\varepsilon}\left(\sqrt{1-\varepsilon^2}-1\right)}
\end{aligned} \tag{6}$$

where $\alpha = n_I Z_I^2 / n_i Z_i^2$, $\mu_i^* = \nu_{iI} qR/\varepsilon^{3/2} \upsilon_{thi}$ and $\Delta' = d\Delta/dr$, where Δ is the Shafranov shift. The impurity thermal conductivity is obtained by interchanging the i and I subscripts in the above expressions.

The Shafranov shift parameter may be evaluated from[34]

$$\Delta' \equiv \frac{d\Delta}{dr} = -\frac{1}{RB_\theta^2}\left(\frac{r^3}{a^2}\beta_\theta B_{\theta a}^2 + \frac{1}{r}\int_o^r B_\theta^2 r' dr' \right) \tag{7}$$

where $\beta_\theta = p/(B_\theta^2/2\mu_0)$ and $B_{\theta a}$ denotes the poloidal magnetic field evaluated at $r = a$. Since we need this quantity at $r \approx a$, we can take advantage of the definition of the internal inductance

$$l_i = \frac{2\int_o^a B_\theta^2 r' dr'}{a^2 B_{\theta a}^2} \tag{8}$$

where $\beta_{\theta a}$ denotes the quantity evaluated using the average pressure over the plasma and $B_{\theta a}$. Using a parabola-to-a-power current profile $j(r) = j_0(1 - (r^2/a^2))^v$, for which the ratio of the values of the safety factor at the edge to the center is $q_a/q_0 = v + 1$, and a fit[32]

$l_i = ln(1.65 + 0.89v)$ leads to the simple expression

$$\Delta' = -\frac{a}{R}\left(\bar{\beta}_{\theta a} + \frac{1}{2} l_i\right)$$
$$= -\frac{a}{R}\left(\bar{\beta}_{\theta a} + \frac{1}{2} ln\left(1.65 + 0.89\left(\frac{q_a}{q_o} - 1\right)\right)\right) \qquad (9)$$

In the presence of a strong shear in the radial electric field, the particle banana orbits are squeezed, resulting in a reduction in the ion thermal conductivity by a factor of $S^{-3/2}$, where[35]

$$S = \left|1 - \rho_{i\theta}\left(\frac{d \ln E_r}{dr}\right)\left(\frac{E_r}{\upsilon_{thi} B_\theta}\right)\right| \qquad (10)$$

Here $\rho_{i\theta}$ is the ion poloidal gyroradius.

2. Ion temperature gradient modes

For a sufficiently large ion temperature gradient $\left(L_{Ti} \equiv -T_i/(dT_i/dr) < L_{Ti}^{crit} \simeq 0.1R \approx 0.18\right)$ the toroidal ion temperature gradient (ITG) modes become unstable. This criterion for instability of the ITG modes was satisfied over the edge region of shot 118897 for the times examined except just at the separatrix in the L-mode stage. An estimate of the ion thermal conductivity due to ITG modes is[36]

$$\chi_i^{itg} = \frac{5}{2}\left(\frac{1}{RL_{Ti}}\right)^{1/2}\left(\frac{T_e}{m_i}\right)\left(\frac{m_i}{e_i B}\right)\frac{1}{2}\rho_i \qquad (11)$$

where ρ_i is the gyroradius in the magnetic field B, and $k_\perp \rho_i = 2$ has been used. The parameter $\eta_i = L_{ni}/L_{Ti}$ for shot 118897 is shown in Fig. 9, from which it may be inferred that ITG modes should be present over the entire edge region in this shot, except just inside the separatrix at 1525 and 2140 ms.

3. Drift Alfven modes

Drift Alfven instabilities are driven by collisions and hence become important in the collisional edge plasma. Numerical modeling[37] indicates that ExB shear alone can not stabilize these modes (low collisionality and a steep pressure gradient are also needed). An analytical model[38] which takes these effects into account yields the expression

$$\chi_i^{da} = \chi_i^{gb} \bar{\bar{\chi}}_\perp\left(\beta_\parallel, \nu_n\right)/\sqrt{\mu} \qquad (12)$$

where the ion gyro-Bohm thermal conductivity is $\chi_i^{gb} = \rho_s^2 c_s / L_{pi}$, with $L_{pi} \equiv -p_i/\left(dp_i/dr\right)$,

$$\mu = -k_{\|} L_{pi} \sqrt{m_i T_e / m_e T_i} \simeq \frac{L_{pi}}{qR} \sqrt{m_i T_e / m_e T_i} \tag{13}$$

for $k_{\|} \simeq 1/qR$, and

$$\overline{\overline{\chi}}_{\perp} = \left[\frac{\left(1+\beta_n^2\right)^{-3} + \nu_n^2}{1+\beta_n^2+\nu_n^{4/3}} \right] \tag{14}$$

where

$$\beta_n \equiv \left(\frac{m_i}{m_e}\right)^{1/2} \beta \frac{qR}{L_{pi}}, \quad \beta = \frac{n_e T_e}{B^2/2\mu_0}, \quad \nu_n \equiv \left(\frac{m_i}{m_e}\right)^{1/4} \frac{\left(qRL_{pi}\right)^{1/2}}{\lambda_e} \tag{15}$$

with $\lambda_e = \upsilon_{the} / \nu_{ei}$ being the electron mean free path.

4. Thermal instabilities

In the weak ion-electron equilibration limit, local radial thermal instabilities in the edge ion and electron energy balances are decoupled, and the linear growth rates may be written in the general form[39]

$$\omega = -\frac{2}{3}\left(\chi_0 \left(\nu L_T^{-2} + k_r^2 \right) + \frac{5}{2} \nu \frac{\Gamma_{\perp}}{n} L_T^{-1} - \alpha \right) \tag{16}$$

where the first two terms represent the generally stabilizing effect of heat conduction and convection, respectively, with L_T^{-1} = (-dT/dr)/T for the species in question, $\Gamma_{\perp}$ being the ion or electron particle flux, and ν characterizing the temperature dependence of the underlying thermal conductivity for that species, $\chi_0 \sim T^{\nu}$. We used $\nu = 2.5$, but the results are relatively insensitive to this value. The α-terms represent the generally destabilizing atomic physics and impurity cooling terms in the respective growth rates for the ions

$$\alpha_i = \frac{5}{2}(\nu - 1)\nu_{ion} + \frac{3}{2}\nu_{at}^c \left(\nu - \left[1 + \frac{T_i}{\nu_{at}^c} \frac{\partial \nu_{at}^c}{\partial T_i} \right] \right) - \frac{1}{n}\left(\nu \frac{H_i}{T_i} - \frac{\partial H_i}{\partial T} \right) \tag{17a}$$

and for the electrons

$$\alpha_e = n_z \left(\frac{\nu L_z}{T_e} - \frac{\partial L_z}{\partial T_e} \right) + \nu_{ion} \left\{ \frac{5}{2}(\nu - 1) + \nu \frac{E_{ion}}{T_e} - \left(\frac{3}{2} + \frac{E_{ion}}{T_e} \right) \frac{T_e}{\nu_{ion}} \frac{\partial \nu_{ion}}{\partial T_e} \right\} - \frac{1}{n}\left(\nu \frac{H_e}{T_e} - \frac{\partial H_e}{\partial T_e} \right) \tag{17b}$$

The terms ν_{ion} and ν_{at} are the neutral ionization frequency in the pedestal region and the frequency of charge-exchange plus elastic scattering events involving 'cold' neutrals that have not previously undergone such an event in the pedestal region. E_{ion} is the ionization

energy, and n_z and L_z are the density and radiative emissivity of impurities in the edge pedestal region. H represents any additional heating or cooling in the pedestal.

An estimate of the transport associated with such thermal instabilities is

$$\Delta\chi_{i,e}^{ti} \simeq \omega k_r^{-2} \tag{18}$$

In evaluating this expression we used $k_r = 5$ m^{-1}, corresponding to radial instabilities with wavelengths of 20 cm, which is about the depth into the plasma that destabilizing neutral and/or impurity radiation effects might penetrate in the L-mode plasma (similar results are obtained for $k_r = 10$ m^{-1} corresponding to 10 cm neutral penetration and radiation zone). We used the neoclassical and paleoclassical values of the ion and electron thermal diffusivities to evaluate χ_0.

B. Electron transport

1. Paleoclassical

A model based on classical electron heat conduction along field lines and magnetic field diffusion in which the electron temperature equilibrates within a distance L along the field lines and in which radially diffusing field lines carry this equilibrated temperature with them and thus induce a radial electron heat transport $M \simeq L/\pi qR \sim 10$ times larger than the resistive magnetic field diffusion rate leads to the following expression for the electron heat diffusivity[40]

$$\chi_e^{paleo} = 1.5(1+M)\frac{\eta_{\|}^{nc}}{\eta_0}\nu_e\delta_e^2 \tag{19}$$

where taking L as the minimum of the electron collision mean free path and the maximum half length of the helical field results in

$$M = \min\{\ell_{\max}, \lambda_e\}/\pi Rq \tag{20}$$

where

$$\delta_e^2\nu_e = \frac{1.4x10^3 Z_{eff}}{T_e^{3/2}(eV)}\left(\frac{\ln\Lambda}{17}\right), \quad \delta_e = c/\omega_{pe}, \ ,$$

$$\ell_{\max} \equiv \pi Rq_* n_{\max} = \frac{\pi Rq_*}{\left(\pi\bar{\delta}_e\frac{dq}{d\rho}\right)^{1/2}} = \frac{R\sqrt{\pi q}}{\left(\frac{\delta_e}{a}\left(\frac{1}{q}\frac{dq}{d\rho}\right)\right)^{1/2}},$$

$$\frac{\eta_{\parallel}^{nc}}{\eta_0}=\left[\frac{\sqrt{2}+Z_{eff}}{\sqrt{2}+13Z_{eff}/4}\right]+\left[\frac{\sqrt{2}+Z_{eff}-\ln(1+\sqrt{2})}{Z_{eff}\left(1+\nu_{*e}^{1/2}+\nu_{*e}\right)}\right]\frac{(1-f_c)}{f_c},$$

$$\nu_{*e}=Rq/\varepsilon^{3/2}\lambda_e,\ f_c=\frac{\left(1-\varepsilon^2\right)^{-1/2}(1-\varepsilon)^2}{1+1.46\varepsilon^{1/2}+0.2\varepsilon},\ \lambda_e=\frac{1.2x10^{16}T_e^2\,(eV)}{n_eZ_{eff}}\left(\frac{17}{\ln\Lambda}\right) \tag{21}$$

2. Electron temperature gradient modes

The electron temperature gradient (ETG) modes (electrostatic drift waves with $k_\perp c_s \le \omega_{pe}$) are unstable when $\eta_e \equiv L_n/L_{Te} \ge 1$, which is the case in the edge region for shot 118897, as shown in Fig. 9. An expression for the thermal conductivity due to the ETG modes is given by[34]

$$\chi_e^{etg}=0.13\left(\frac{c_s}{\omega_{pe}}\right)^2\frac{\upsilon_{the}S_m}{qR}\eta_e\left(1+\eta_e\right) \tag{22}$$

where $S_m \equiv (r/q)(dq/dr)$ is the magnetic shear and ω_{pe} is the electron plasma frequency.

3. Trapped Electron Modes

The principal electron drift instabilities with $k_\perp c_s \le \Omega_i$ arise from trapped particle effects when $\nu_e^* \equiv \nu_e/(\upsilon_{the}/qR)\varepsilon^{3/2} < 1$. In more collisional plasmas the mode becomes a collisional drift wave destabilized by passing particles. An expression for the electron thermal diffusivity that encompasses the dissipative trapped electron mode (TEM) and the transition to the collisionless mode as $\nu_e^* \to 0$ is given by[34]

$$\chi_e^{tem}=0.13\left(\frac{c_s}{\omega_{pe}}\right)^2\frac{\upsilon_{the}\left(\frac{r}{q}\frac{dq}{dr}\right)}{qR}\eta_e\left(1+\eta_e\right) \tag{23}$$

4. Drift Resistive Ballooning Mode

The drift-resistive ballooning mode is destabilized by unfavorable curvature on the outboard side of the torus in a collisional edge plasma. Linear stability analysis[41]

indicates that the transport associated with these modes can be characterized by a particle diffusion coefficient scaling $D \sim (2\pi q)^2 \rho_e^2 \nu_{ie} (R/L_n)$ and a proportionality constant equal to the flux surface average of the normalized fluctuating radial particle flux $<nV_r>$. Subsequent calculation[42] of the normalized fluctuating radial particle fluxes for model representative of DIII-D core parameters found $<nV_r> \approx 0.01\text{-}0.05$. We adopt the form

$$\chi_e^{rb} = 4 \frac{R}{L_n} (q\rho_e)^2 \nu_e \qquad (24)$$

to characterize the transport of electron energy due to drift-resistive ballooning modes, with the caveat that there could well be an additional normalization constant needed. We note that one group of transport modelers[43] calibrated this formula to L-mode data and found a factor of $94\kappa^{-4}$ should multiply this expression (κ is the elongation), while another group[44] used this expression multiplied by a factor of 4.

VI. Comparison of theoretical predictions with inferred thermal diffusivities

The theoretical expressions of the previous section were evaluated using the measured density and temperatures and are compared with the values inferred from experiment using Eq. (2) in Figs. 10 and 11.

The agreement of the thermal instability prediction for ion thermal diffusivity (Fig. 10a) and of the paleoclassical prediction for electron thermal diffusivity (Fig. 11a) with the experimentally inferred profiles for the L-mode (1525 ms) is notable. The etg prediction is of the same magnitude as the experimentally inferred $\chi_e^{\exp}$, but the profiles differ significantly.

For the H-mode the itg prediction agrees reasonably well with $\chi_i^{\exp}$ in the early, transient phase (Fig. 10b), but at later times the neoclassical prediction agrees better at the inner radii, but both neoclassical and itg predict a sharp decrease in χ_i at the outer radii that is not seen in $\chi_i^{\exp}$. The presence of drift Alfven instability could account for addition χ_i needed to match $\chi_i^{\exp}$ at the outer radii. It is notable that the ion thermal instability was stabilized except at the inner radii by the steeper temperature gradient in the H-mode than in the L-mode.

The experimentally inferred $\chi_e^{\exp}$ profiles for the H-mode are well under all the theoretical predictions (Figs. 11b and 11c). As noted previously, there is uncertainty in

the magnitude to be used for the resistive ballooning mode expression, but a reduction in magnitude would not change the disagreement in shape. It seems unlikely that any of the theoretical mechanisms considered are responsible for the inferred χ_e^{exp}.

VI. Summary and Discussion

The ion and electron thermal diffusivities in the edge region have been inferred from density and temperature profile measurements during the fully developed L-mode stage, during an early transient H-mode stage and during a fully developed H-mode stage of a DIII-D discharge with a long ELM-free H-mode phase. The ion and electron conductive heat flux edge profiles used to evaluate the thermal diffusivities were calculated taking into account radiation, atomic physics effects associated with recycling neutrals, ion-electron collisional equilibration and neutral beam heating in the edge.

The inferred thermal diffusivities for both ions and electrons decreased by about an order of magnitude between the L-mode and ELM-free H-mode stages of the discharge, as anticipated. This decrease occurred across the entire outer 15% of the plasma minor radius, not just in the localized regions in the outer 5% where the steep-gradient pedestals in density and temperature formed in the H-mode. There was a broad (width about 5% of minor radius) minimum in χ_e^{exp} centered at about 95% of the minor radius in the H-mode stages, even though the steepness of the measured T_e gradient increased with radius up to within less than 1% of the minor radius.

Comparison of $\chi_{e,i}^{exp}$ with theoretical predictions found reasonably good agreement in the L-mode stage for the paleoclassical prediction of χ_e and the thermal-instability prediction of χ_i. In the H-mode stages, the broad minimum in the inferred χ_e^{exp} was well under any of the theoretical predictions (paleoclassical, etg, tem, resistive ballooning). The inferred χ_i^{exp} agreed reasonably well with the itg prediction (and not quite so well with the neoclassical prediction) of χ_i early in the H-mode stage, but χ_i^{exp} was significantly larger than either of these predictions in the outer 4% of the minor

radius later in the H-mode stage. The resistive ballooning mode prediction of χ_i agreed with $\chi_i^{\exp}$ in magnitude but not in profile over this outer 4% of the minor radius.

ACKNOWLEDGEMENTS: The authors are grateful to members of the DIII-D team who performed the experiments and measured and reduced the data discussed in this paper. The first author (WMS) is grateful to Glen Bateman, Jim Callen, Parvez Gudzar, and Alexie Pankin for discussion and clarification of certain aspects of the theoretical models and to General Atomics for their hospitality during the course of this work. The work was supported by the US Dept. of Energy through grant DE-FG02-99ER54538 with the Georgia Tech Research Corporation and contract DE-AC03-99ER54463 with General Atomics.

REFERENCES

1. R. J. Groebner and T. H. Osborne, Phys. Plasmas, 5, 1800 (1998).
2. A. E. Hubbard, R. L. Boivin, R. S. Granetz, *et al.*, Phys. Plasmas, 5, 1744 (1998).
3. W. Suttrop, O. Gruber, B. Kurzan, *et al*., Plasma Phys. Control. Fusion, 42, A97 (2000).
4. T. H. Osborne, J. R. Ferron, R. J. Groebner, *et al*., Plasma Phys. Control Fusion, 42, A175 (2000).
5. A. E. Hubbard, Plasma Phys. Control. Fusion, 42, A15 (2000).
6. J. R. Ferron, M. S. Chu, G. L. Jackson, *et al.*, Phys. Plasmas, 7, 1976 (2000).
7. L. D. Horton, A. V. Chankin, Y. P. Chen, *et al*., Nucl. Fusion, 45, 856 (2005).
8. A. Kallenbach, Y. Andrew, M. Beurskens, *et al.,* Plasma Phys. Control. Fusion, 46, 431 (2004).
9. M. Kotschenreuther, W. Dorland, Q. P. Liu, *et al*., Proceedings of 16th Conference on Plasma Physics and Controlled Fusion Research, Montreal, 1996 (IAEA, Vienna, 1997), Vol. 2, p 371.
10. J. E. Kinsey, R. E. Waltz and D. P. Schissel, Proceedings of 24th European Physical Society Meeting, Berchtesgarten, (EPS, Geneva, 1997) Vol. III, p 1081.
11. R. L. Miller, Y. R. Lin-Liu, T. H. Osborne and T. S. Taylor, Plasma Phys. Control. Fusion, 40, 753 (1998).
12. J. W. Connor, R. J. Hastie, H. R. Wilson and R. L. Miller, Phys. Plasmas, 5, 2687 (1998).
13. H. R. Wilson and R. L. Miller, Phys. Plasmas, 6, 873 (1999).
14. P. B. Snyder, H. R. Wilson, J. R. Ferron, *et al*., Phys. Plasmas, 9, 2037, (2002); also Nucl. Fusion, 44, 320 (2004).
15. R. J. Groebner, M. A. Mahdavi, A. W. Leonard, *et al*., Phys. Plasmas, 9, 2134 (2002); also Nucl. Fusion, 44, 204 (2004).
16. W. M. Stacey, Phys. Plasmas, 11, 1511 (2004); also 11, 4295 (2004); also 11, 5487 (2004).
17. W. M. Stacey and R. J. Groebner, Phys. Plasmas, 12, 042504 (2005); also 13, 012513 (2006).
18. C. S. Chang, S. Ku and H. Weitzner, Phys. Plasmas, 11, 2649 (2004).
19. G. D. Porter, R. Isler, J. Boedo and T. D. Rognlien, Phys. Plasmas, 7, 3663 (2000).

20. D. P. Coster, X. Bonnin, K. Borrass, *et al.*, Proceeding of 18th Fusion Energy Conference, Sorrento, Italy, 2000 (IAEA, Vienna, 2001).
21. T. Onjun, G. Bateman, A. Kritz, *et al*., Phys. Plasmas, 9, 5018 (2002).
22. W. M. Stacey and R. J. Groebner, Phys. Plasmas, 10, 2412 (2003).
23. B. Scott, Plasma Phys. Control. Fusion, 39, 1635 (1997).
24. T. D. Rognlien, X. Q. Xu and R. H. Cohen, Plasma Phys. Control. Fusion, 42, A271 (2000).
25. W. M. Stacey and R. J. Groebner, Phys. Plasmas, 13 (July, 2006).
26. W. M. Stacey, Phys. Plasmas, 5, 1015 (1998); also 8, 3673 (2001); also Nucl. Fusion, 40, 965 (2000).
27. W. M. Stacey, E. W. Thomas and T. M. Evans, Phys. Plasmas, 2, 3740 (1995); also 4, 678 (1997).
28. R. Hulse, Nucl. Technol./Fusion, 3, 259 (1983).
29. T. N. Carlstrom, G. L. Campbell, J. C. DeBoo, *et al.*, Rev. Sci. Instrum., 63, 4901 (1992).
30. P. Gohil, K. H. Burrell, R. J. Groebner, *et al.*, Proceeding of 14th Symposium on Fusion Engineering, San Diego, 1991 (Inst. Electrical & Electronics Engineers, New York, 1992) Vol 2, 1199 .
31. T. K. Kurki-Suonio, R. J. Groebner, and K. H. Burrell, Nucl. Fusion, 32, 133 (1992).
32. C. S. Chang and F. L. Hinton, Phys. Fluids, 25, 1493 (1982).
33. C. S. Chang and F. L. Hinton, Phys. Fluids, 29, 3314 (1986).
34. J. A. Wesson, *Tokamaks,* 2nd ed. (Clarendon Press, Oxford, 1997).
35. K. C. Shaing and R. D. Hazeltine, Phys. Fluids B, 4, 2547 (1992).
36. F. Romanelli, W. M. Tang and R. B. White, Nucl. Fusion, 26, 1515 (1986).
37. B. N. Rogers, *et al.*, Phys. Rev. Lett., 81, 4396 (1998).
38. W. Kerner, Contrib. Plasma Phys., 38, 118 (1998).
39. W. M. Stacey, Phys. Plasmas, 6, 2452 (1999).
40. J. D. Callen, Nucl. Fusion, 45, 1120 (2005).
41. D. R. McCarthy, P. N. Gudzar, J. F. Drake, *et al*., Phys. Fluids B, 4, 1846 (1992).
42. P. N. Gudzar, J. F. Drake, D. R. McCarthy, *et al*., Phys. Fluids B, 5, 3712 (1993).
43. G. Bateman, A. H. Kritz, J. E. Kinsey, *et al*., Phys. Plasmas, 5, 1793 (1998).
44. D. Kalupin, M. Z. Tokar, B. Unterberg, *et al*., Nucl. Fusion, 45, 468 (2005).

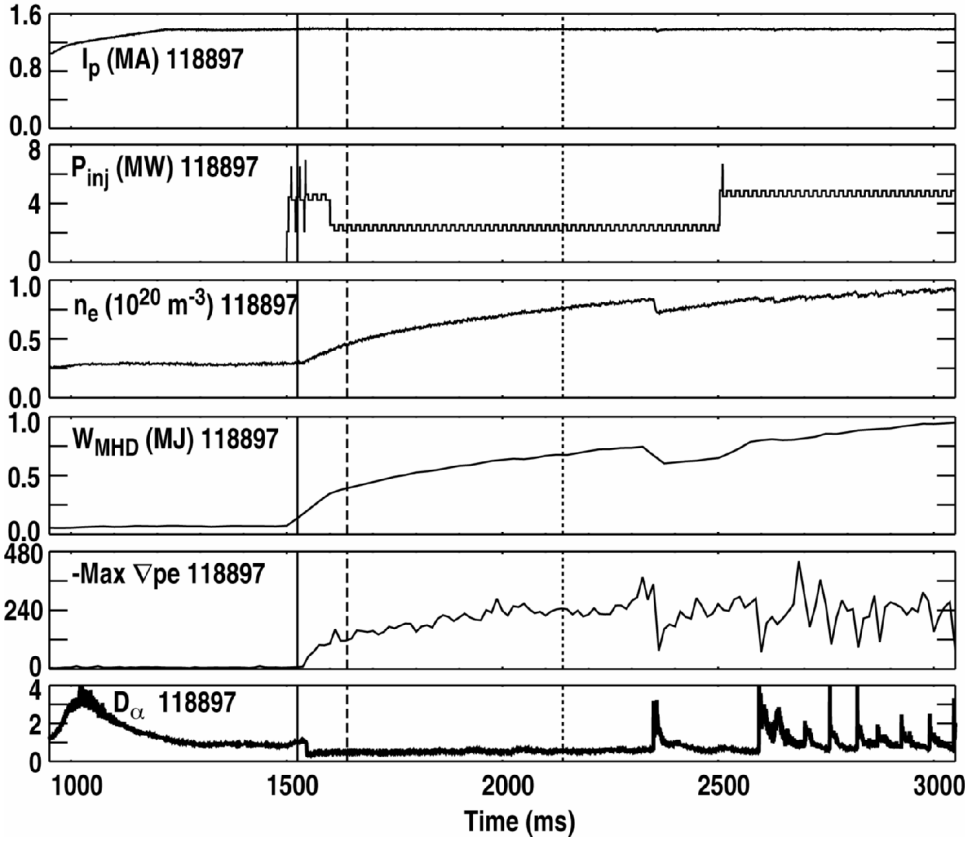

Figure 1. Evolution of measured parameters in DIII-D shot 118897. (The pressure gradient is measured [in kPa/m] along the vertical chord of the Thomson lasers and would be approximately a factor of two higher when projected to the outboard midplane.)

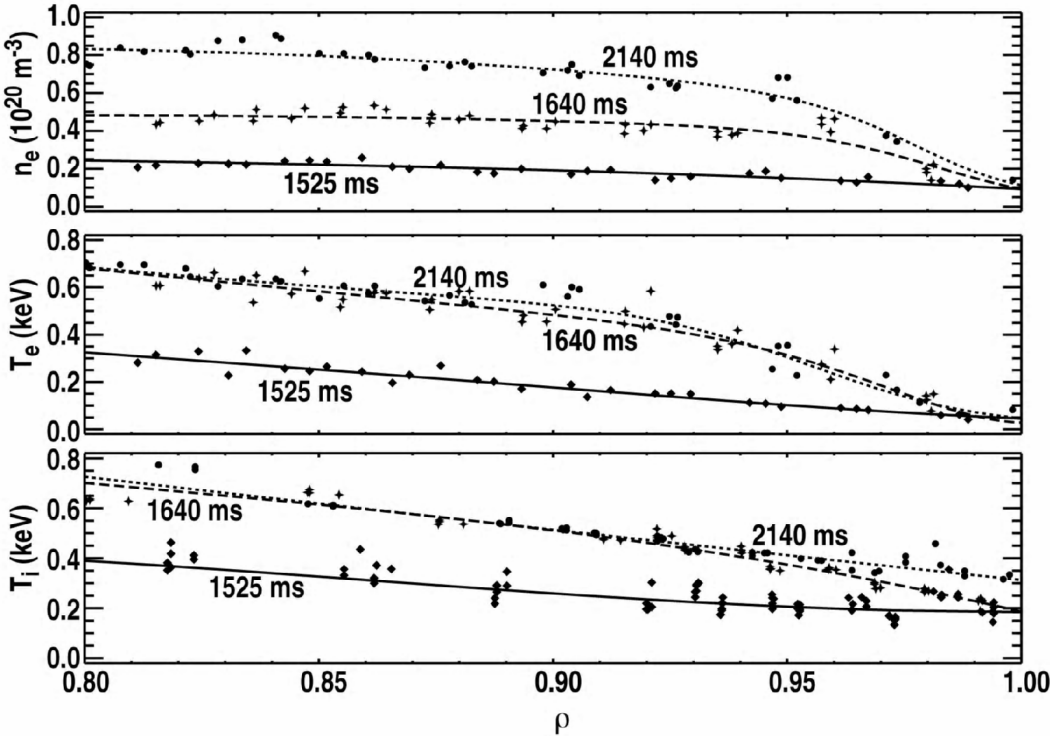

Figure 2. Measured and fitted densities and temperatures in the edge of DIII-D shot 118897.

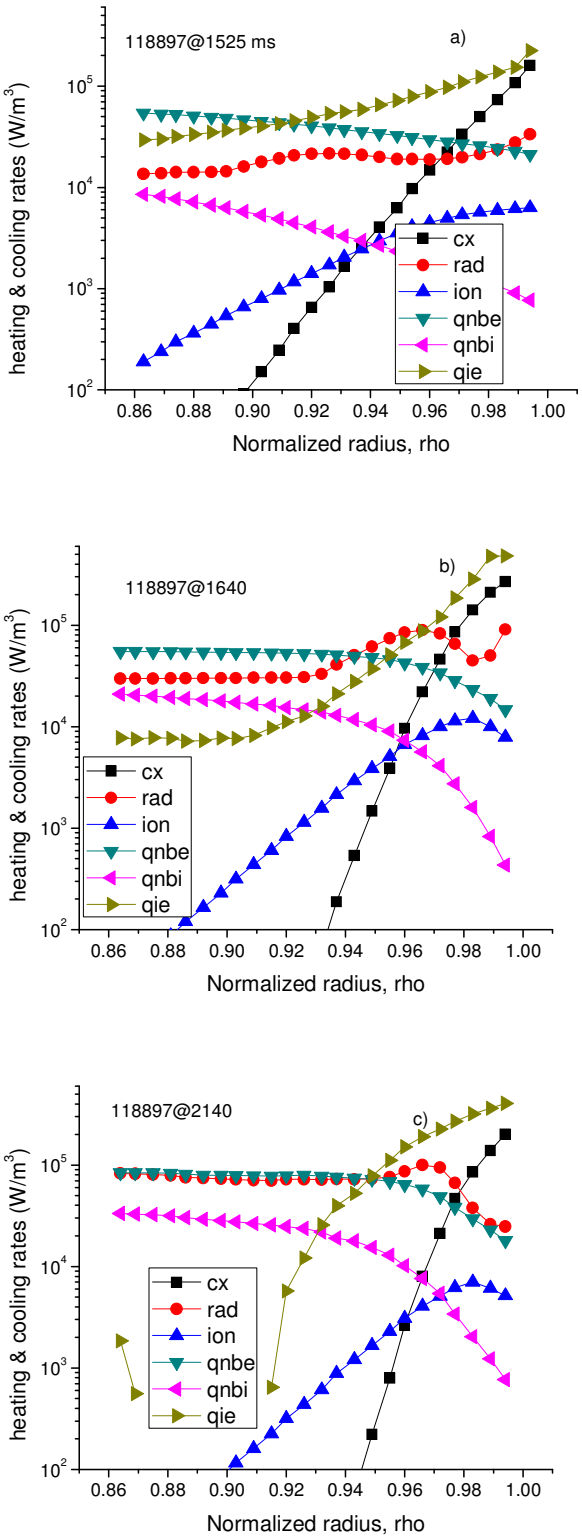

Figure 3. Heating and cooling rates a) just before L-H with P_{nb}=4.45 MW, b) just after L-H with P_{nb}= 2.33 MW, and c) well after L-H with P_{nb}=2.33 MW. (cx=charge-exchange+elastic scattering cooling, rad=radiation cooling, ion=ionization cooling, qnbe=neutral beam heating of electrons, qnbi = neutral beam heating of ions, qie=collisional energy exchange from ions to electrons)

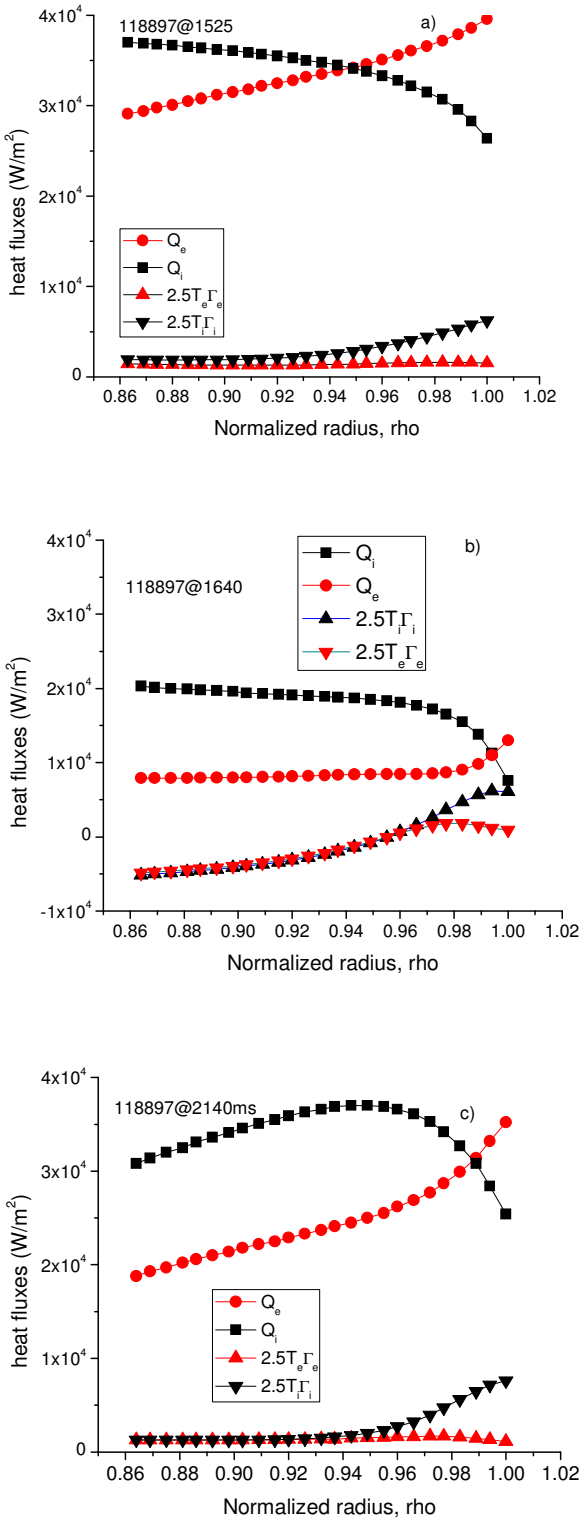

Figure 4. Total and convective heat fluxes a) just before L-H with P_{nb} = 4.45 MW, b) just after L-H with P_{nb}= 2.33 MW, and c) well after L-H with P_{nb} = 2.33 MW. (heate,i=total heat flux, heatconve,i=convective heat flux)

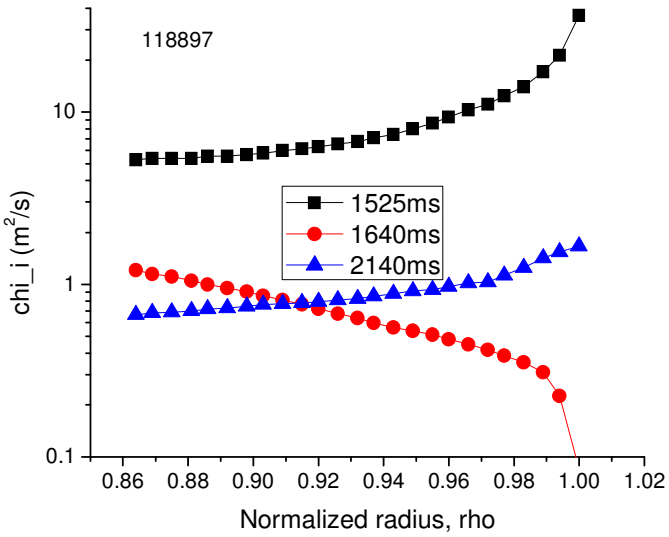

Figure 5. Experimentally inferred ion thermal diffusivity just before L-H (1525ms), just after L-H (1640ms) and well after L-H (2140ms).

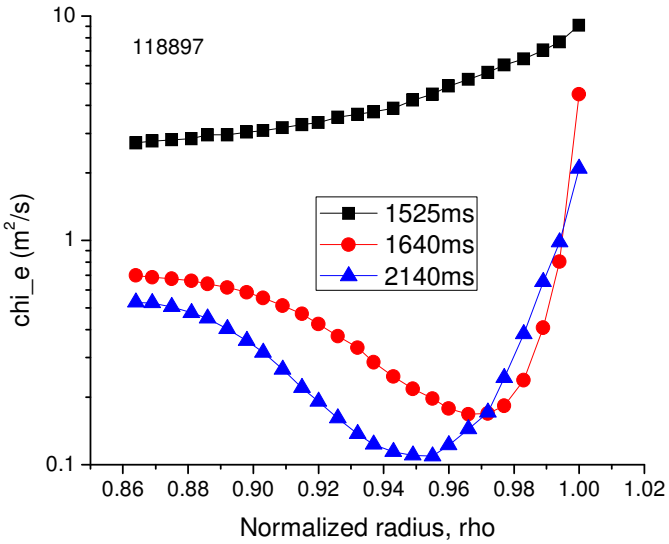

Figure 6. Experimentally inferred electron thermal diffusivity just before L-H (1525ms), just after L-H (1640ms) and well after L-H (2140ms).

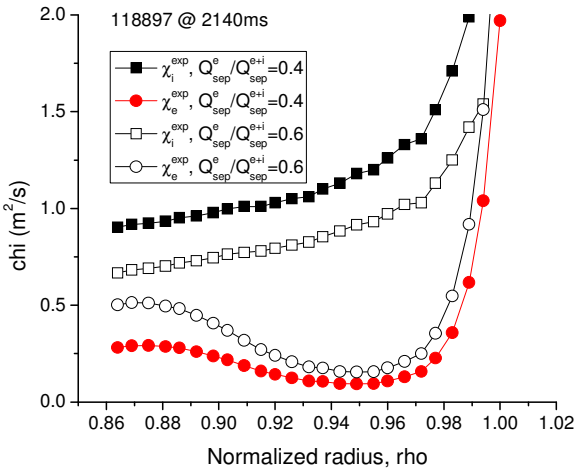

Figure 7. Sensitivity of inferred thermal diffusivity to assumed fheate=$Q_e/(Q_e+Q_i)$ leaving the core (@ ρ = 0.864).

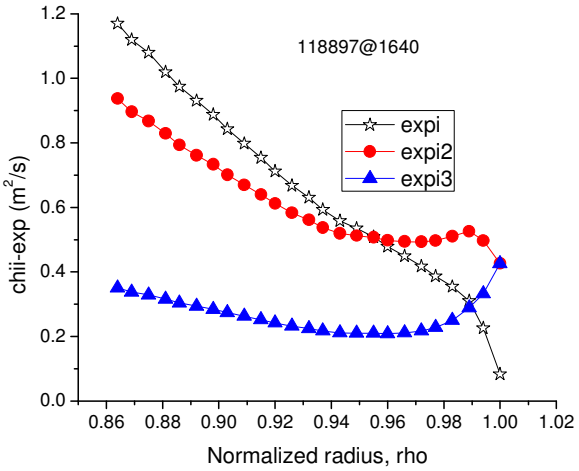

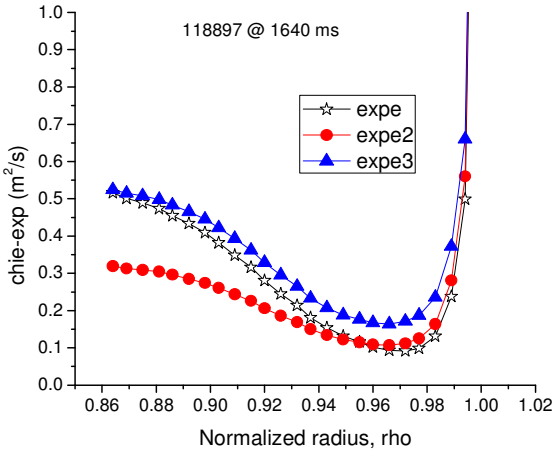

Figure 8. Sensitivity of inferred thermal diffusivity to heat flux. ('exp' used conductive heat flux q(r)=Q(r)-2.5Γ(r)T(r); 'exp2' used total heat flux Q(r); and 'exp3' used constant value of total heat flux at separatrix $Q(r_{sep})$.

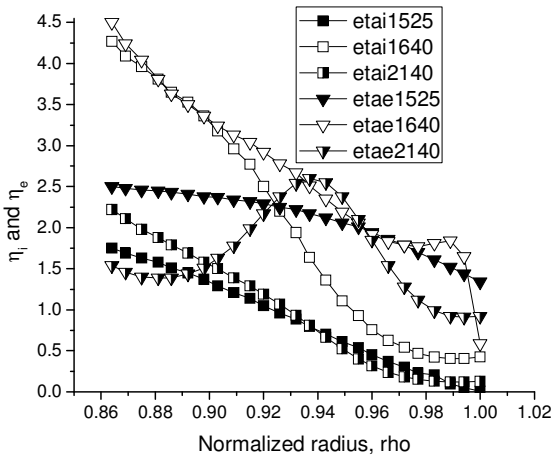

Figure 9. $\eta_{e,i} \equiv L_{ne,i} \big/ L_{Te,i}$ for DIII-D shot 118897.

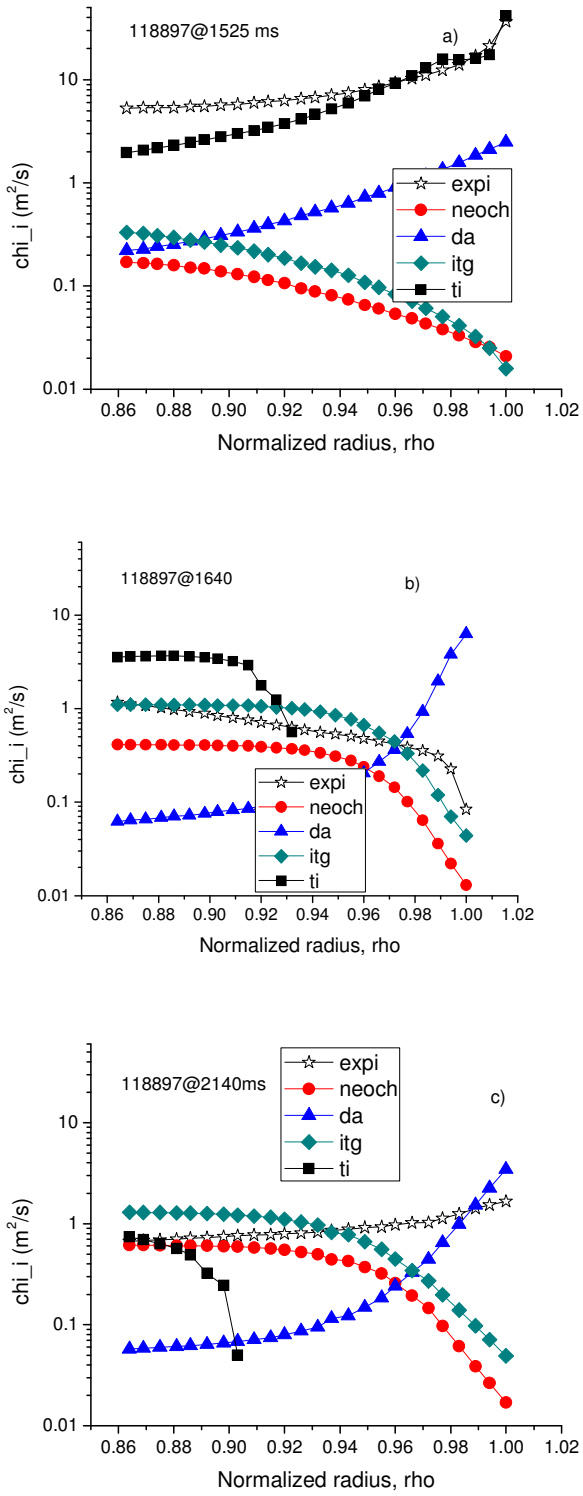

Figure 10. Comparison of experimentally inferred ion thermal diffusivities with theoretical predictions a) just prior to L-H, b) just after L-H, and c) well after L-H. (expi=inferred from exp., neoch=neoclassical Chang-Hinton, da= drift Alfven mode, itg=ion temperature gradient mode, ti= thermal instability)

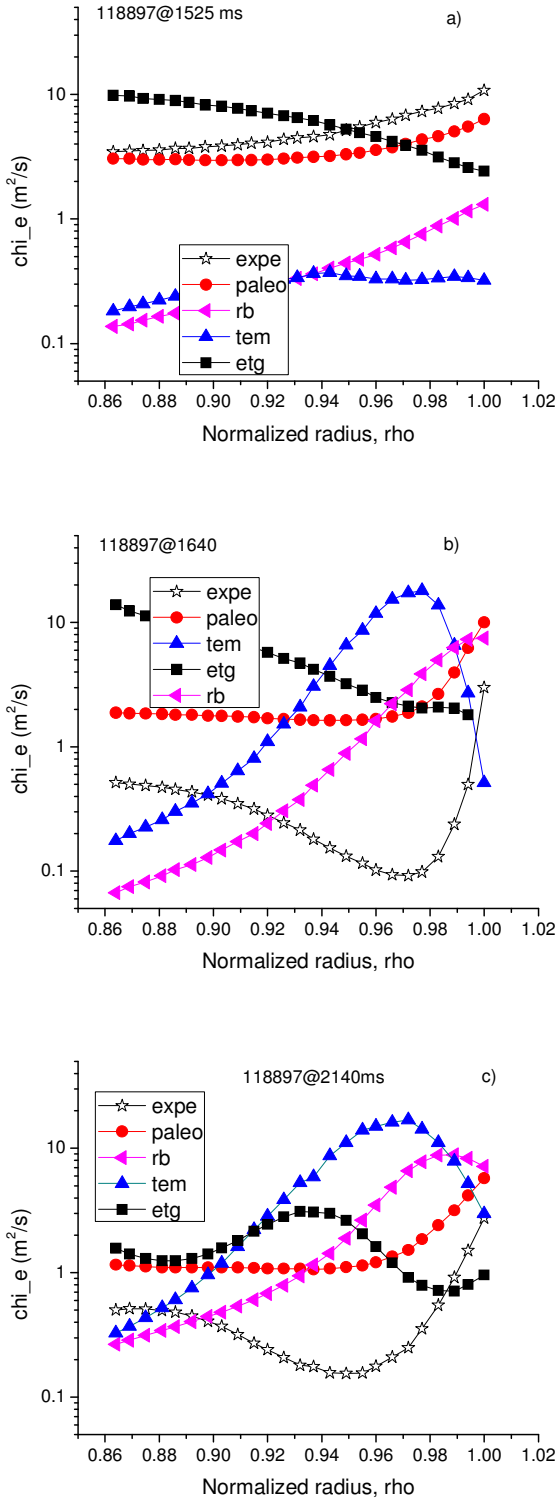

Figure 11. Comparison of experimentally inferred electron thermal diffusivities with theoretical predictions a) just prior to L-H, b) just after L-H, and c) well after L-H. (expe=inferred from exp., paleo=paleoclassical, rb= resistive ballooning mode, tem=trapped electron mode, etg=electron temperature gradient mode)